Electronic Supplementary Information

Identifying the roles of acid-base sites in formation pathways of tolualdehydes from acetaldehyde over MgO-based catalysts

Marcella Lusardi,† Thomas Struble,‖ Andrew Teixeira,‡ Klavs F. Jensen†,‖,*

†Materials Science and Engineering, Massachusetts Institute of Technology, Cambridge, Massachusetts 02139 USA
‖Chemical Engineering, Massachusetts Institute of Technology, Cambridge, Massachusetts 02139 USA
‡Chemical Engineering, Worcester Polytechnic Institute, Worcester, Massachusetts 01609 USA
*Corresponding Author: kfjensen@mit.edu

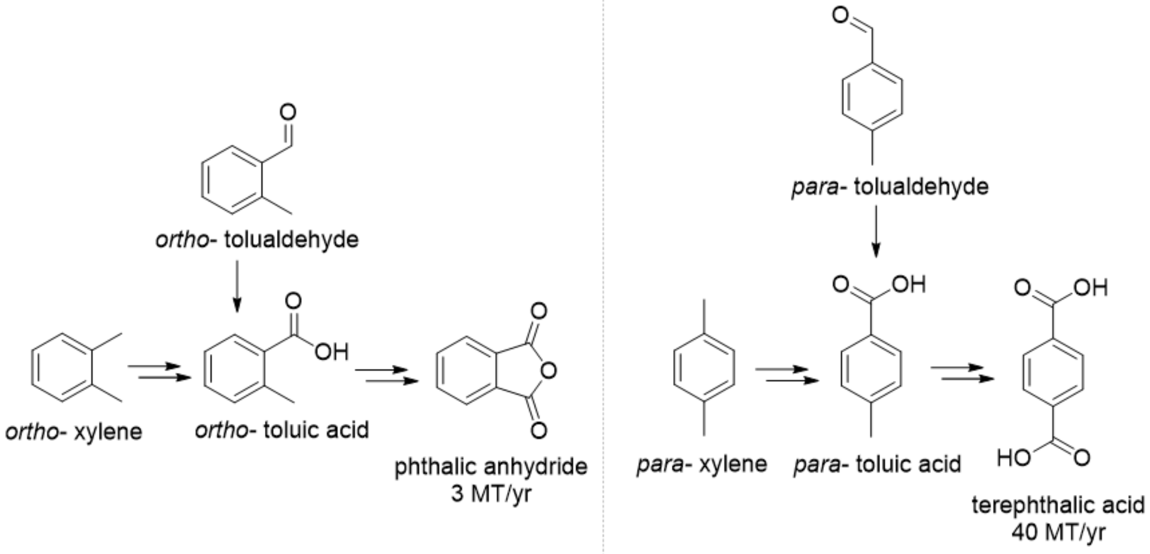

Scheme S1. Overview of aromatic monomer production from xylenes and facile xylenes substitution by tolualdehydes

Tolualdehydes are partially oxidized xylenes. Because the first step in the production of phthalic anhydride and terephthalic acid involves the oxidation of xylenes to toluic acids,[1,2] tolualdehydes are viable xylene replacements in the synthesis of these aromatic monomers.

Details of the co-precipitation synthesis:

To 50 mL of deionized (DI) water under a N_2 atmosphere, $Mg(NO_3)_3\cdot 6H_2O$ and $Al(NO_3)_3\cdot 9H_2O$ were added such that the desired molar Mg/Al ratios (2 and 3, corresponding to Al fractions of 0.33 and 0.25, respectively) and a total metal cation concentration $[Mg^{2+} + Al^{3+}] = 1.2\ M$ were achieved. This solution was added dropwise under vigorous stirring to a round bottom flask containing 150 mL of DI water and Na_2CO_3. The amount of Na_2CO_3 added was determined from the amount of charge-compensating CO_3^{2-} anions necessary to balance the excess positive charge in the LDH layers due to the Al^{3+} incorporation ($[CO_3^{2-}] = 0.5\ [Al^{3+}]$), taken with a 20% excess. The pH was maintained at 10 by co-feeding a 2 *M* solution of NaOH dropwise to the round bottom flask. After the addition was complete, the solution was statically aged in an oil bath at 75 °C for 18 hours. The formed precipitate was vacuum filtered and washed with copious amounts of DI water until the pH of the filtrate reached 7. The LDH was then dried overnight at 80 °C. Pure $Mg(OH)_2$ and $Al(OH)_3$ were synthesized using the same recipe with only $Mg(NO_3)_3\cdot 6H_2O$ and $Al(NO_3)_3\cdot 9H_2O$, respectively.

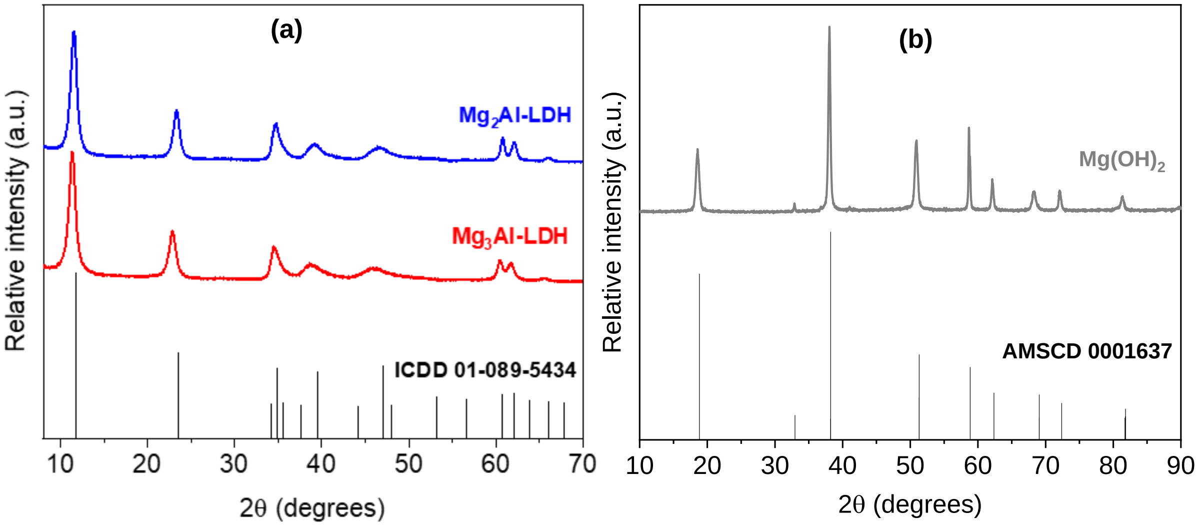

Figure S1. XRD patterns for (a) the Mg-Al layered double hydroxides (Mg_xAl-LDH) and (b) $Mg(OH)_2$.

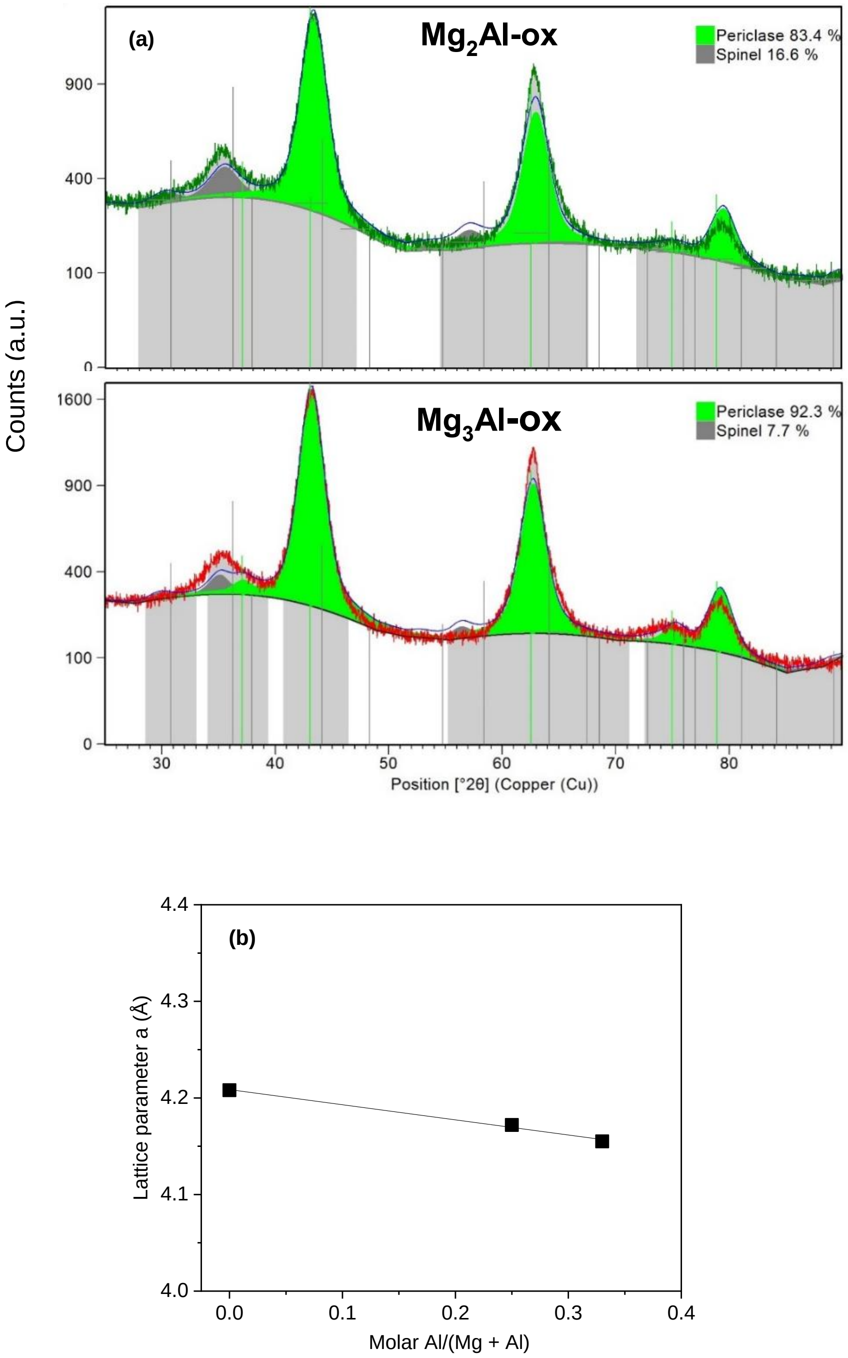

Figure S2. (a) Rietveld refinement of the XRD patterns with experimental (dark green and red) and calculated (lime for periclase, dark gray for spinel) curves and calculated phase (periclase, spinel-type) fractions. Goodness of fit values were between 2.2 and 2.3. (b) The lattice parameter *a,* calculated from the diffraction angle of the (200) plane in periclase, the Miller indices of this plane, and Bragg's Law, linearly decreases with increasing Al content due to the smaller radius of Al (0.535 Å) compared to Mg (0.720 Å). This indicates that Al isomorphically substitutes for Mg in the periclase phase.[3,4]

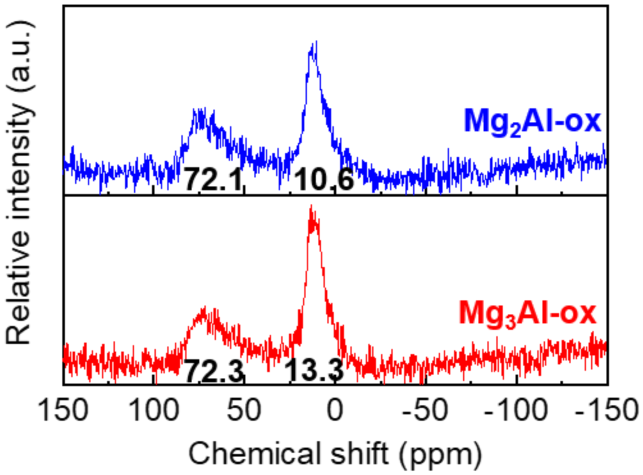

Figure S3. ^{27}Al MAS NMR spectra for Mg_xAl-ox show two broad resonances attributed to octahedral and tetrahedral Al^{3+}. Chemical shift values (in ppm) are labeled under each resonance. In the periclase phase,

Al_O arises from the isomorphic substitution of Mg^{2+} with Al^{3+}, while Al_T comes from Al incorporation into the tetrahedral holes of the FCC lattice—during calcination of the Mg-Al LDH, some of the Al_O in the brucite-like layers reduces to tetrahedral coordination to alleviate the bonding loss at the onset of layer dehydroxylation.[5,6] The spinel-type phase can have both Al_O and Al_T coordination environments, depending on the degree of inversion.[3,7] The chemical shift for Al is sensitive to the second nearest neighbor (NN) coordination sphere; AlO_Y polyhedra (where y = 4 or 6 for tetrahedral or octahedral coordination, respectively) bonded to Mg (AlO_Y-Mg) have second NNs with a lower electron density, and thus experience weaker shielding effects, than those bonded to Al (AlO_Y-Al), resulting in larger positive chemical shift values for AlO_Y-Mg.[7] Thus, we would expect Al coordinated in the periclase phase, with a higher degree of Mg second NNs, to result in resonances downfield relative to those in the spinel-type phase, which have a higher degree of Al NNs. This trend is clearly observed for Mg_3Al-ox, which has the lower Al content and the smaller spinel phase fraction, giving the more positive chemical shift values. Al_O and Al_T are shielded to differing degrees in Mg_2Al-ox (upfield for Al_O—influenced more by spinel, downfield for Al_T). The absence of peak splitting to represent the distinct coordination environments possible in each phase make further analysis and quantification of the catalytically-relevant periclase phase not possible in these Mg_xAl-ox samples.

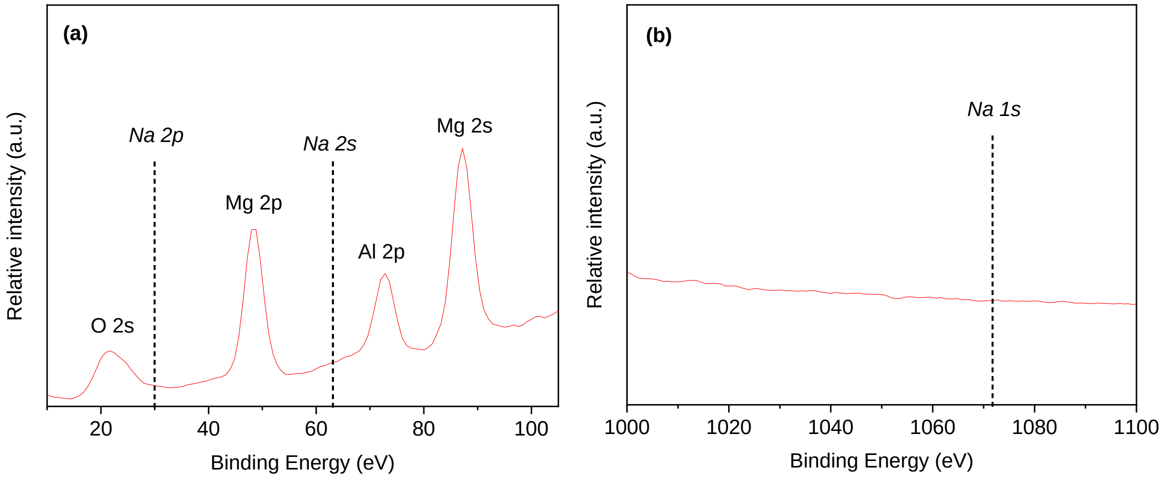

Figure S4. XPS analysis on Mg_3Al-ox as a representative sample shows the absence of Na signals near (a) 30 and 63 eV and (b) 1072 eV,[8,9] indicating no measurable Na^+ content on the surface.

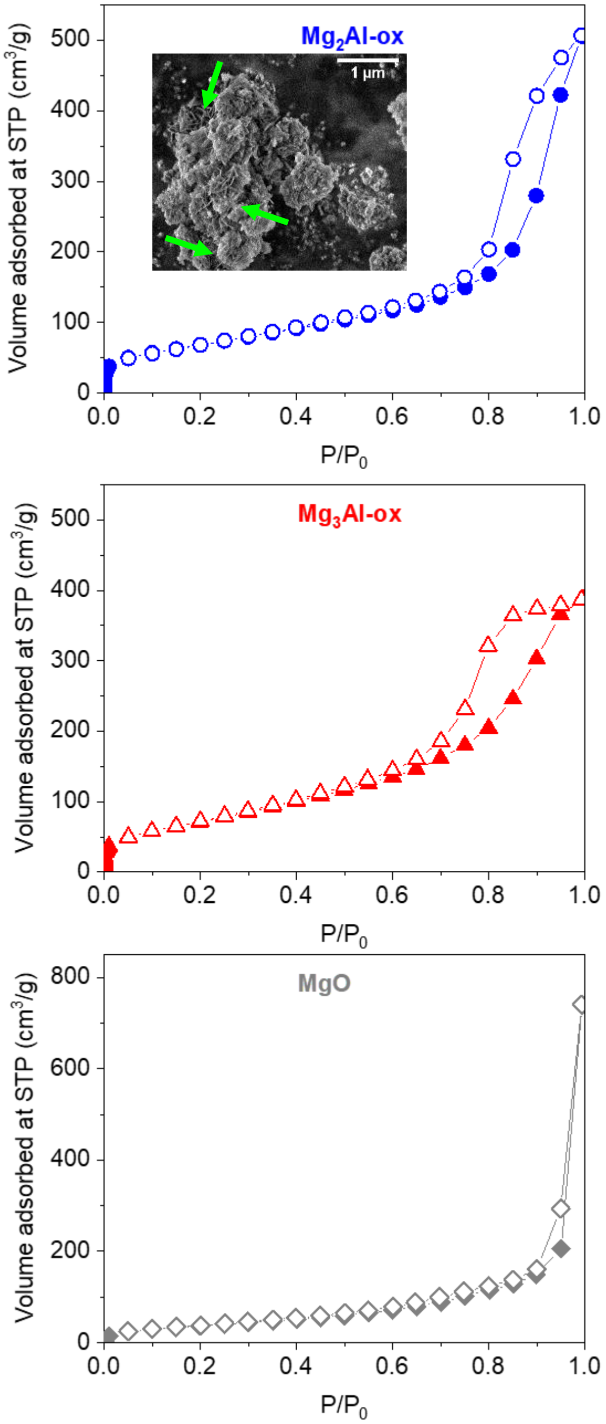

Figure S5. N_2 adsorption (solid symbols) and desorption (open symbols) isotherms measured at 77K for the Mg_xAl-ox and MgO catalysts. Inset in isotherm for Mg_2Al-ox shows aggregation of platelet-shaped crystallites that give rise to slit-shaped mesopores.

The isotherms for Mg_xAl-ox are of type IV and exhibit type H3 hysteresis, which is consistent with the presence of slit-shaped mesopores that form from the aggregation of platelet-shaped crystallites (SEM image in inset of Fig. S5) during calcination and decomposition of the LDH phase.[10–12] The MgO sample exhibits a type II isotherm, which indicates that the accessible surface of this oxide is dominated by macroporosity and/or external surface area.[10]

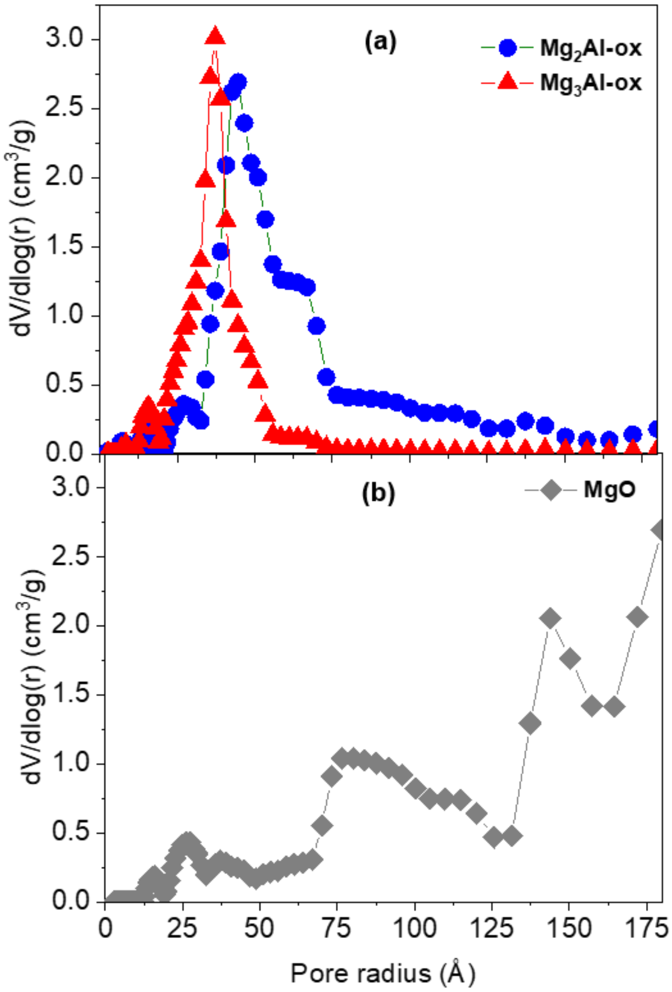

Figure S6. DFT pore size distributions calculated from the N_2 adsorption-desorption isotherms (77 K) for (a) Mg_xAl-ox and (b) MgO.

The DFT pore size distributions (PSDs) for Mg_xAl-ox show the presence of mesopores predominantly between 3 and 15 nm in diameter (d_{pore}) as well as micropores with d_{pore} ~1.5 nm, which form from gaseous CO_2 and H_2O “cratering” through the decomposing layers during calcination.[13,14] The PSD for MgO shows the presence of a wide distribution of mesopores (d_{pore} between 3 and 35 nm).

Discussion of the results from the CO_2 TPD experiments over the oxide catalysts

Probe molecule TPD experiments are sensitive to several factors, including the sweep gas flowrate, the temperature ramp, and molecular diffusion of the probe through the catalyst pores. These effects preclude precise identification of specific (e.g., weak vs. medium) site types as a function of desorption temperature, but general trends can be observed, and the total site density can be measured. CO_2 desorption from weak and medium strength sites manifests in a broad peak for the Mg_xAl-ox samples at lower temperatures. Weak basic sites arise from surface hydroxylation of the metal oxide (M-O) upon dissociative adsorption of H_2O (OH/M^{x+} and H/O^{2-}), with the latter hydroxyl group acting as a weak Brønsted base.[15] The larger amount of CO_2 desorption from Mg_2Al-ox compared to Mg_3Al-ox (T ~ 125 ˚C) suggests the former has a larger density of weakly basic hydroxyl groups. This might originate during the decomposition of the LDH precursors. As the structure decomposes during calcination, interlayer carbonate anions and water molecules react to form gaseous CO_2 and hydroxyl groups to coordinate with octahedral M^{n+}.[16] The density of these charge-compensating carbonates increases with Al content in the LDH phase, resulting in a more hydroxylated environment that can persist even after calcination.[17]

Medium strength sites arise from M-O pairs exposed on the {100} surface.[5] While the site strengths are comparable (i.e., the desorption occurs over the same temperature range) for the Mg_xAl-ox samples, the density of sites with 200 ˚C < T_{desorb} < 450 ˚C decreases with increasing Al content. Further, the maximum for the peak corresponding to desorption from weak/medium-strength sites shift to 325 ˚C over Mg_3Al-ox compared to Mg_2Al-ox (225 ˚C), indicating a higher density of relatively stronger medium-strength sites over the Mg_3Al-ox sample. This is consistent with the fact that stoichiometric periclase surfaces with more Mg-O domains will have stronger medium-strength, M-O-type basic sites than those with higher degrees of Al coordination, due to the higher electron density on an oxygen coordinated to Mg^{2+} compared to that coordinated to the more electronegative Al^{3+}.[5,18] Additionally, we observe a trend in overall basic character in the decreasing total basic site density with increasing Al content (Table 1).

The lower temperature region in the profile for pure MgO shows distinct desorption events centered around 250 and 325 °C. These basic sites are very similar in nature to those on the Al-substituted oxides: weakly basic hydroxyl groups form from water dissociation on the M-O surface, and medium strength sites arise from surface-exposed M-O pairs. However, the pure MgO is a single phase and has fewer inherent defects (e.g., no heteroatom substitution or tetrahedral occupation), making for a more crystalline structure. This, in turn, yields a narrower distribution of sites compared to the complex coordination environments in the Al-substituted samples.

The peaks at higher temperature (>450 ˚C) in the Mg_xAl-ox and MgO TPD profiles can be attributed to CO_2 desorption from strong sites. Strong basic centers form from low-coordinated O^{2-}, which can have unsaturated bonding due to morphology (e.g., edges or corners) or other defects (e.g., cation vacancies).[5] It is also possible that some of the desorption at these higher temperatures over the Al-substituted samples arises from the decomposition of remnant carbonates that grafted into the oxide structure during calcination of the LDH phase.[17]

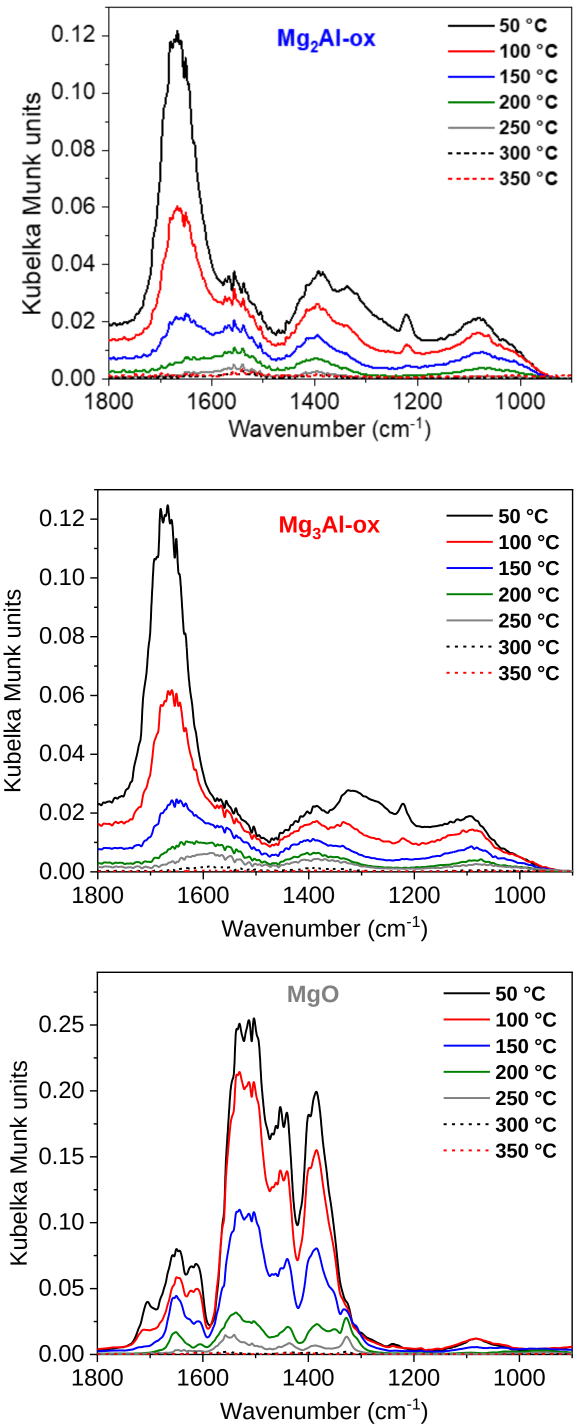

Figure S7. DRIFTS spectra of CO_2 adsorbed on Mg_xAl-ox and MgO measured from 50 to 350 ˚C.

Kubelka Munk units = $f(R_\infty)$[19]

$$R_\infty(T) = \frac{R^{CO_2}_{sample}(T)}{R^{He}_{sample}(T)}$$

$$f(R_\infty(T)) = \frac{(1 - R_\infty(T))^2}{2R_\infty(T)}$$

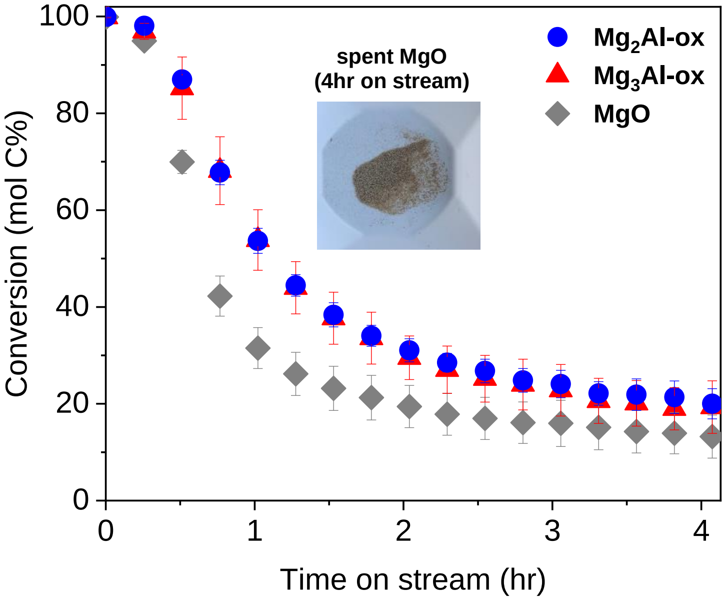

Figure S8. Acetaldehyde conversion profiles over Mg_xAl-ox and MgO (0.1% acetaldehyde/99.9% N_2, 10 sccm total flowrate, 10 mg catalyst, 250 ˚C, 1 bar) show a steep decay indicative of catalyst deactivation. Inset shows the brown color of the spent MgO sample after 4 hr on stream (fresh sample is white). Spent Mg_xAl-ox exhibited similar color changes (not shown).

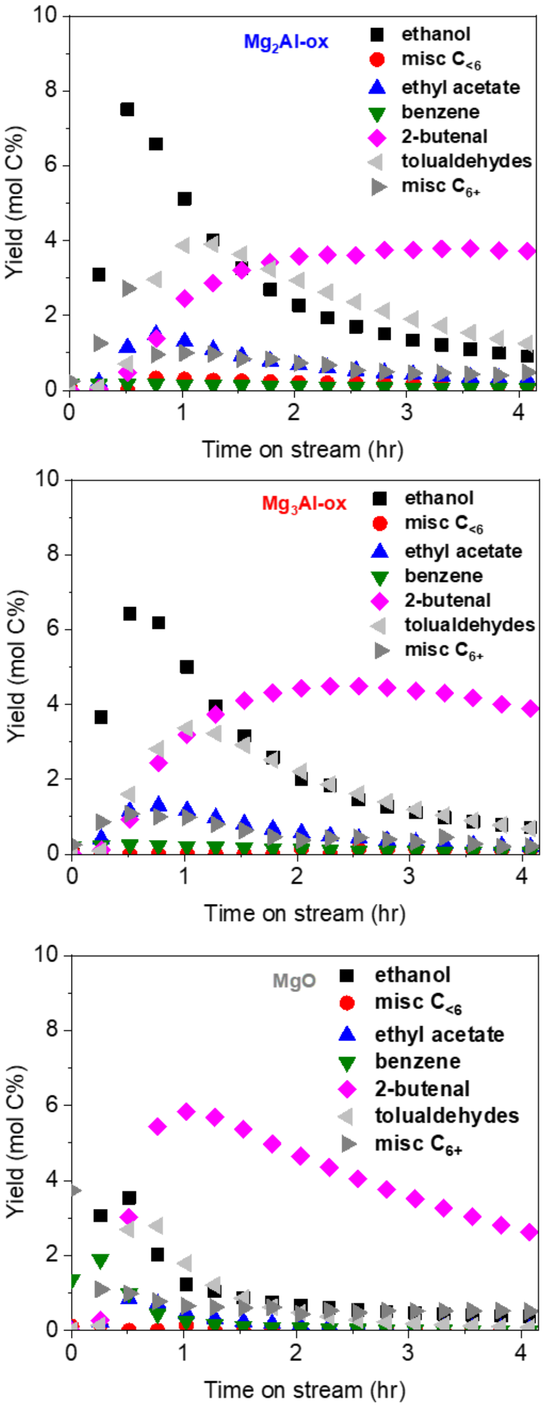

Figure S9. Full product distributions measured over time for the Mg$_x$Al-ox and MgO catalysts (0.1% acetaldehyde/99.9% N$_2$, 10 sccm total flowrate, 10 mg catalyst, 250 ˚C, 1 bar).

Ethanol can be produced from acetaldehyde via gas-phase hydrogenation/reduction reactions over metal oxide catalysts (e.g., SiO_2-supported alkali metals,[20] faujasite-type zeolites,[21] MgAl and NiAl oxides,[22] TiO_2 surfaces[23]) that exhibit basic character. The hydrogen required for this can be produced from the decomposition of acetaldehyde[22,23] or water[24] (generated as a by-product during condensation reactions), or from the formation of heavy carbonaceous deposits (via dehydration and dehydrogenation routes) that form at early time on stream. Other work has suggested that ethanol is produced from acetaldehyde via a Cannizzarro-type disproportionation, despite the fact that this mechanism usually requires a non-enolizable (i.e., lacking α-H) aldehyde.[25–27] We do not detect the formation of acetic acid, a by-product of a Cannizzarro-type disproportionation, but we do detect trace amounts of acetone that can form from acetate coupling over basic metal oxides.[28] Either mechanism could be contributing.

The largest amounts of ethanol were measured over the Mg_xAl-ox catalysts. These catalysts have more acid-strong base pairs than MgO (minimal acidity) that facilitate the formation of ethoxide species from acetaldehyde.[5,20,23] For Cannizzaro-type disproportionation reactions, these sites facilitate the adsorption (Lewis acid rather than vacancy-mediated), nucleophilic attack, and hydrogen transfer in the proposed mechanism.[26]

Ethanol can also be produced from the Claisen condensation or hydrolysis of ethyl acetate, which forms from the Tischenko esterification of two acetaldehyde molecules.[24,29] We detect ethyl acetate formation at early times on stream that has previously been reported to occur over acid-base pairs (increasing with increasing catalyst acidity).[21,29,30] However, the ethyl acetate yields were not sensitive to CO_2 titration while ethanol yields were (see Fig. S11). If ethyl acetate was an intermediate for ethanol production, we would expect an increase in ethyl acetate yields as ethanol formation activity decreased. Thus, direct hydrogenation/reduction or Cannizzarro-type reactions are responsible for ethanol formation. No major ethanol-derived products were detected in the product stream (e.g., 2-methylbenzyl alcohol, the alcohol analog of *ortho*-tolualdehyde/2-methylbenzaldehyde). The surface coverage of ethanol is likely much less than that of acetaldehyde given that the latter is continuously fed into the reactor, and the residence time is quite short (~10 ms).[31]

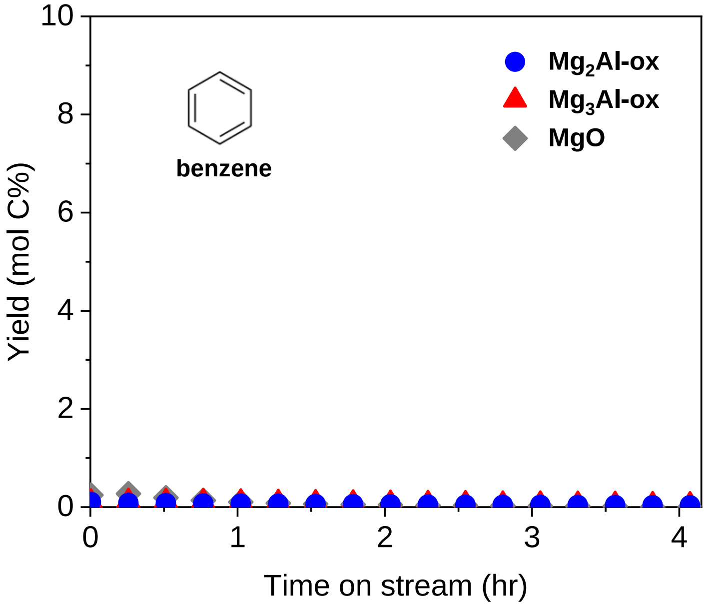

Figure S10. Benzene yields over Mg$_x$Al-ox and MgO with strong basic sites (low-coordinated O^{2-}) titrated by CO$_2$ (0.1% acetaldehyde/10 % CO$_2$/89.9% N$_2$, 10 sccm total flowrate, 10 mg catalyst, 250 ˚C, 1 bar).

Over untreated MgO (Fig. 4b), the benzene yield peaks within the first 0.5 hr on stream, and then decays to 0. Benzene activity over Mg$_x$Al-ox samples is negligible (<0.2 mol C%). The low overall activity on all catalysts could be due to unfavorable kinetics (i.e., less favorable than competitive pathways), rapid active site deactivation, and/or low density of active sites. Benzene forms via the cross-condensation of acetaldehyde and 2-butenal (Scheme S2). The C$_2$ α-enolate formed via base deprotonation (red arrow) adding to the C$_4$ carbonyl-C is shown, but the same product (2,4-hexadienal) can theoretically be obtained from the C$_4$ enolate (at the γ-C) adding to the C$_2$ carbonyl-C. Upon dehydration of the aldol, 2,4-hexadienal forms. This cyclodehydrates via a ring-closing mechanism to benzene.[21] The production of benzene must compete with several other pathways. First, 2,4-hexadienal can be an intermediate to 2,4,6-octatrienal in a cross condensation with acetaldehyde. This would consume 2,4-hexadienal to yield the tertiary aldol product. However, our analysis from the production of the C$_8$ species indicates that this is likely not a primary factor contributing to the low benzene yields. 2,4-hexadienal is produced through either base-deprotonation of the acetaldehyde α-C or 2-butenal γ-C, followed by addition to the carbonyl-C positions on 2-butenal or acetaldehyde, respectively. This addition step (cross-condensation) competes with the same (α-C$_2$ or γ-C$_4$) enolates adding to the carbonyl-C positions on acetaldehyde or 2-butenal, respectively, which would form 2-butenal and 2,4,6-octatrienal and/or *o*-tolualdehyde (self-condensation). Thus, it is possible the self-condensation routes are more kinetically favorable relative to the cross condensation-route required to form 2,4-hexadienal and ultimately, benzene. Additionally, if the C$_2$ α-enolate is forming more appreciably than the C$_4$ γ-enolate, the probability of its interaction with the carbonyl-C of acetaldehyde is much higher than that of 2-butenal: a continuous feed of 1000 ppm (0.1%) acetaldehyde is delivered to the reactor.

In-situ CO_2 titration studies, which selectively deactivate basic sites whose temperature of CO_2 desorption exceeds that of the reaction temperature (250 ˚C), show that strong basic sites are responsible for early TOS benzene activity over MgO. Thus, over MgO, strong basic sites attributed to low-coordinated surface O^{2-} are the responsible sites for benzene formation at early TOS, before MgO promotes other aldol pathways and/or the site deactivates. Deactivation is likely, given the tendency of strong basic sites to produce heavy polycondensation-type products that are nonvolatile at reaction conditions, resulting in fast deactivation due to site blockage.[32–34] No significant change in benzene activity is detected over the CO_2-titrated Mg_xAl-ox strong sites, which indicates that the low benzene activity on these materials arises from weak and/or medium strength sites. These catalysts and/or reaction conditions are not good candidates for further analysis of benzene formation given the very low overall benzene production.

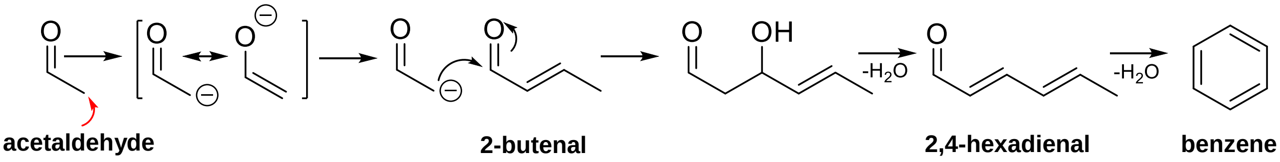

Scheme S2. Formation of benzene via cross-aldol condensation of acetaldehyde and 2-butenal and cyclodehydration of the 2,4-hexadienal aldol product

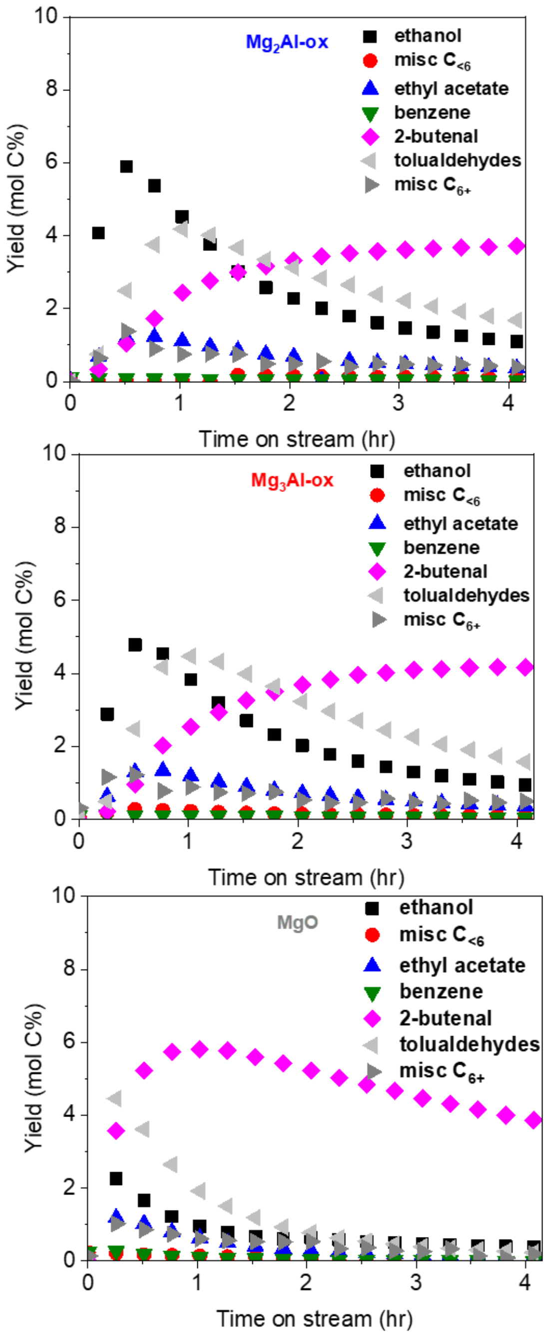

Figure S11. Full product distributions measured over time for the *in-situ* CO_2-titrated Mg_xAl-ox and MgO catalysts (0.1% acetaldehyde/10 % CO_2/89.9% N_2, 10 sccm total flowrate, 10 mg catalyst, 250 ˚C, 1 bar).

In-situ CO_2 titration minimally affects ethyl acetate production, consistent with previous reports that acid-base pairs (rather than low-coordinated O^{2-}) are predominantly responsible for the Tischenko esterification of acetaldehyde.[21,22,29,30] Ethanol production (particularly at early time on stream) is also affected, because of the influence of the strong sites on the intermediates, rather than the actual formation mechanism, involved in ethanol production (similar to the effect of CO_2 pretreatment on tolualdehyde yields). *In-situ* CO_2 titration impacts ethanol formation not because strong O^{2-} sites are responsible (otherwise, we would see complete loss of ethanol production), but because the selective deactivation of these sites thwarts their role in the formation of heavy carbonaceous deposits, the by-product of which is H_2. Decreased gas-phase H_2 then decreases the extent of acetaldehyde hydrogenation/reduction. While strong, low-coordinated O^{2-} sites do participate in certain mechanisms,[35,36] medium-strength, M-O pairs on MgO surfaces are the active center for the formation of the primary side products (ethanol, ethyl acetate) measured in this study.[20,21,23,26,29,30] As a result, selective deactivation of strong, O^{2-} sites does not significantly impact the product distribution.

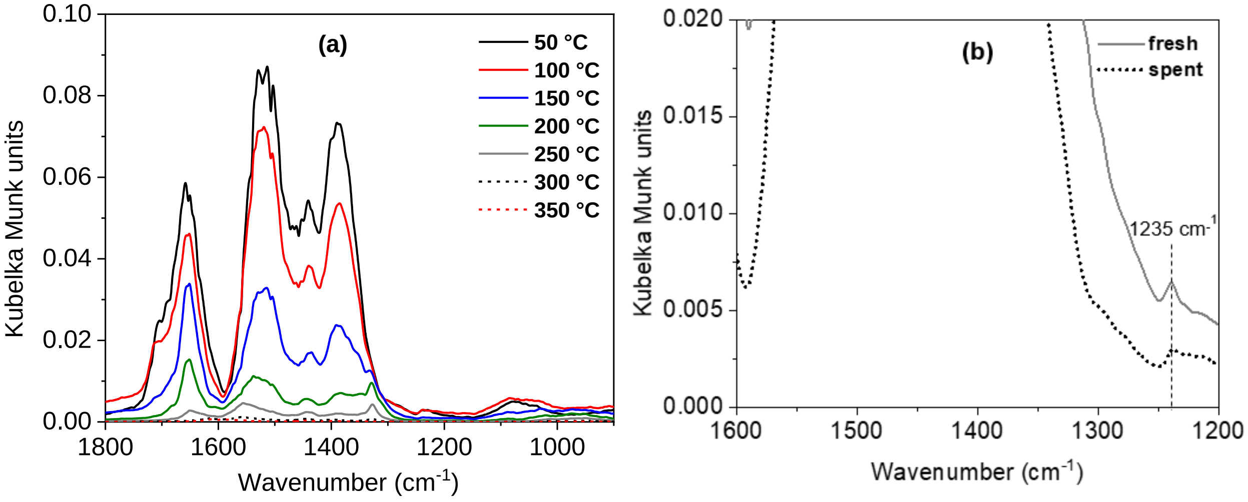

Figure S12. (a) CO_2 DRIFTS spectra from 50 to 350 ˚C on spent MgO, after 5 hr on stream. Time on stream determined by the time to reach tolualdehyde yields <0.001 mol C%. (b) CO_2 DRIFTS spectra on fresh and spent MgO at 100 ˚C, zoomed in to 0.02 Kubelka Munk units to more clearly visualize the low-intensity δ(C-OH) mode.

Table S1. Equilibrium distribution of tolualdehyde isomers (*ortho-* and *para-*) at 250 ˚C, 1 bar calculated in ASPEN

Tolualdehyde isomer	x^{eq} (mol/mol)
ortho-	0.312
para-	0.688

Results found to be independent of initial molar fraction guess, total concentration of tolualdehydes in gas feed, and reactor module (REquil/RGibbs).

Table S2. Computational details for NBO analysis of acetaldehyde

Acetaldehyde

Smiles CC(=O)

Input

```
----------------------------------------------------------------------
 # opt freq=noraman b3lyp/6-311+g(d,p) pop=(hirshfeld,nbo,savenbo,full)
  iop(3/33=4) geom=connectivity temperature=523 K
 ----------------------------------------------------------------------
```

Optimized Coordinates

O	-1.2342380000	-0.2763090000	0.0000280000
C	-0.2335470000	0.3965810000	-0.0001070000
C	1.1682080000	-0.1483230000	0.0000140000
H	-0.3074530000	1.5065110000	0.0002120000
H	1.1639890000	-1.2381520000	-0.0000370000
H	1.7046170000	0.2262410000	0.8788950000
H	1.7047800000	0.2263230000	-0.8787310000

Energies	**Units: [Hartree/Particle]**
Zero-point correction=	0.055177
Thermal correction to Energy=	0.06417
Thermal correction to Enthalpy=	0.065826
Thermal correction to Gibbs Free Energy=	0.00608
Sum of electronic and zero-point Energies=	-153.82697
Sum of electronic and thermal Energies=	-153.817977
Sum of electronic and thermal Enthalpies=	-153.816321
Sum of electronic and thermal Free Energies=	-153.876068

Table S2, continued

NBO analysis

Summary of Natural Population Analysis:

```
                          Natural Population
          Natural  -----------------------------------------------
  Atom  No    Charge        Core      Valence    Rydberg      Total
 --------------------------------------------------------------------
    O    1   -0.52648     1.99976     6.50999    0.01673     8.52648
    C    2    0.43776     1.99957     3.52410    0.03857     5.56224
    C    3   -0.68254     1.99934     4.67504    0.00815     6.68254
    H    4    0.09841     0.00000     0.89735    0.00424     0.90159
    H    5    0.22333     0.00000     0.77434    0.00233     0.77667
    H    6    0.22476     0.00000     0.77366    0.00158     0.77524
    H    7    0.22475     0.00000     0.77367    0.00158     0.77525
 ======================================================================
  * Total *   -0.00000     5.99867    17.92815    0.07318    24.00000
```

Table S3. Computational details for NBO analysis of 2-butenal

2-butenal (Crotonaldehyde)

Smiles CC=CC=O

Input

```
---------------------------------------------------------------------
 # opt freq=noraman b3lyp/6-311+g(d,p) pop=(hirshfeld,nbo,savenbo,full)
  iop(3/33=4) geom=connectivity temperature=523 K
 ---------------------------------------------------------------------
```

Optimized Coordinates

O	-2.4668530000	-0.2518810000	0.0000020000
C	-1.4039430000	0.3318140000	-0.0000020000
C	-0.0916850000	-0.3248290000	-0.0000010000
C	1.0413570000	0.3902540000	0.0000010000
C	2.4274760000	-0.1652550000	0.0000000000
H	-1.3692690000	1.4433680000	-0.0000030000
H	-0.0880330000	-1.4113180000	-0.0000030000
H	0.9580170000	1.4772790000	0.0000020000
H	2.4301420000	-1.2565380000	-0.0000020000
H	2.9823700000	0.1851740000	0.8773880000
H	2.9823710000	0.1851790000	-0.8773850000

Energies	**Units: [Hartree/Particle]**
Zero-point correction=	0.089113
Thermal correction to Energy=	0.103707
Thermal correction to Enthalpy=	0.105364
Thermal correction to Gibbs Free Energy=	0.031014
Sum of electronic and zero-point Energies=	-231.217519
Sum of electronic and thermal Energies=	-231.202925
Sum of electronic and thermal Enthalpies=	-231.201269
Sum of electronic and thermal Free Energies=	-231.275618

Table S3, continued

```
Summary of Natural Population Analysis:

                              Natural Population

            Natural  -----------------------------------------------

  Atom  No    Charge         Core      Valence    Rydberg      Total

 ---------------------------------------------------------------------

    O    1   -0.53107     1.99977    6.51647    0.01484     8.53107

    C    2    0.39127     1.99943    3.56952    0.03978     5.60873

    C    3   -0.30903     1.99899    4.29119    0.01884     6.30903

    C    4   -0.08663     1.99914    4.07181    0.01568     6.08663

    C    5   -0.61810     1.99933    4.60828    0.01048     6.61810

    H    6    0.10045     0.00000    0.89553    0.00402     0.89955

    H    7    0.21011     0.00000    0.78629    0.00360     0.78989

    H    8    0.18975     0.00000    0.80781    0.00244     0.81025

    H    9    0.21080     0.00000    0.78766    0.00155     0.78920

    H   10    0.22122     0.00000    0.77729    0.00148     0.77878

    H   11    0.22122     0.00000    0.77729    0.00148     0.77878

 =======================================================================

   * Total *    0.00000     9.99666   27.88914    0.11420    38.00000
```

Table S4. Computational details for NBO analysis of 2,4-hexadienal

2,4-hexadienal (Sorbaldehyde)

Smiles CC=CC=CC=O

Input

```
--------------------------------------------------------------------
 # opt freq=noraman b3lyp/6-311+g(d,p) pop=(hirshfeld,nbo,savenbo,full)
  iop(3/33=4) geom=connectivity temperature=523 K
 --------------------------------------------------------------------
```

Optimized Coordinates

O	3.6973890000	-0.2109520000	0.0000050000
C	2.6096830000	0.3302080000	-0.0000040000
C	1.3290460000	-0.3733030000	-0.0000030000
C	0.1601010000	0.3011220000	0.0000000000
C	-1.1530700000	-0.3026560000	-0.0000010000
C	-2.2941240000	0.4071270000	0.0000010000
C	-3.6717160000	-0.1715500000	0.0000010000
H	2.5325320000	1.4397320000	-0.0000060000
H	1.3642070000	-1.4589010000	-0.0000040000
H	0.1949050000	1.3904840000	0.0000010000
H	-1.1989230000	-1.3897490000	-0.0000030000
H	-2.2262180000	1.4942290000	0.0000040000
H	-3.6541890000	-1.2632790000	-0.0000020000
H	-4.2354740000	0.1647110000	-0.8776170000
H	-4.2354730000	0.1647060000	0.8776210000

Energies	**Units: [Hartree/Particle]**
Zero-point correction=	0.122509
Thermal correction to Energy=	0.142998
Thermal correction to Enthalpy=	0.144655
Thermal correction to Gibbs Free Energy=	0.055431
Sum of electronic and zero-point Energies=	-308.610808
Sum of electronic and thermal Energies=	-308.590318
Sum of electronic and thermal Enthalpies=	-308.588662
Sum of electronic and thermal Free Energies=	-308.677886

Table S4, continued

```
Summary of Natural Population Analysis:

                         Natural Population

          Natural  -----------------------------------------------

  Atom  No    Charge        Core      Valence    Rydberg      Total

 ---------------------------------------------------------------------

    O    1   -0.53569     1.99977    6.52112    0.01481     8.53569

    C    2    0.38138     1.99942    3.57962    0.03959     5.61862

    C    3   -0.28821     1.99904    4.27137    0.01779     6.28821

    C    4   -0.13144     1.99909    4.11427    0.01808     6.13144

    C    5   -0.24689     1.99902    4.22931    0.01855     6.24689

    C    6   -0.10369     1.99913    4.08908    0.01547     6.10369

    C    7   -0.61303     1.99934    4.60379    0.00990     6.61303

    H    8    0.09988     0.00000    0.89626    0.00386     0.90012

    H    9    0.20974     0.00000    0.78683    0.00343     0.79026

    H   10    0.19630     0.00000    0.80095    0.00276     0.80370

    H   11    0.19978     0.00000    0.79708    0.00313     0.80022

    H   12    0.18787     0.00000    0.81014    0.00199     0.81213

    H   13    0.20779     0.00000    0.79073    0.00147     0.79221

    H   14    0.21811     0.00000    0.78041    0.00148     0.78189

    H   15    0.21811     0.00000    0.78041    0.00148     0.78189

 =======================================================================

  * Total *   -0.00000    13.99481   37.85138    0.15380    52.00000
```

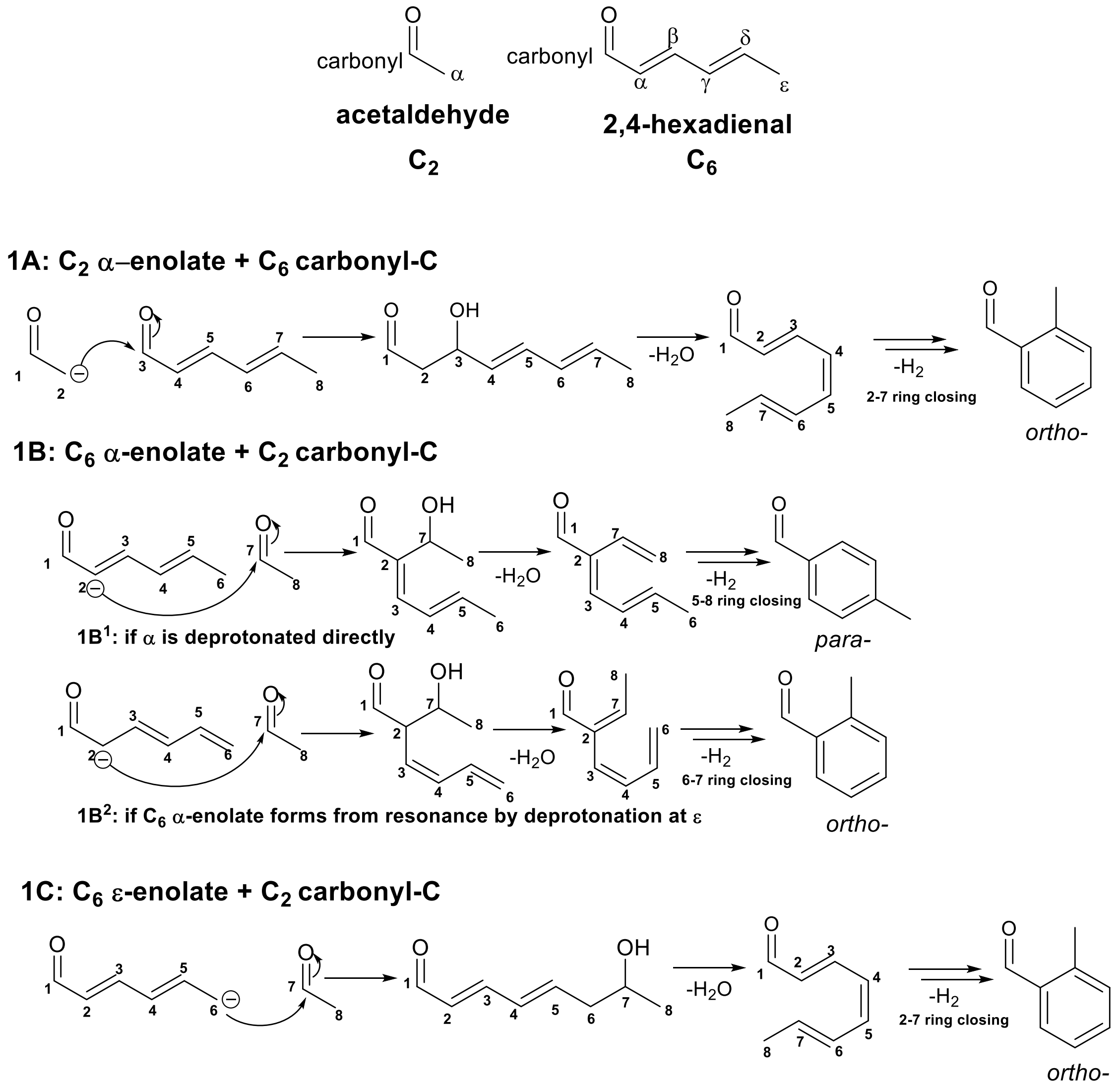

Scheme S3. Proposed route 1 (C_2 + C_6) cross-condensation subroutes that result in C_8 enals that can mechanistically electrocyclize to tolualdehydes

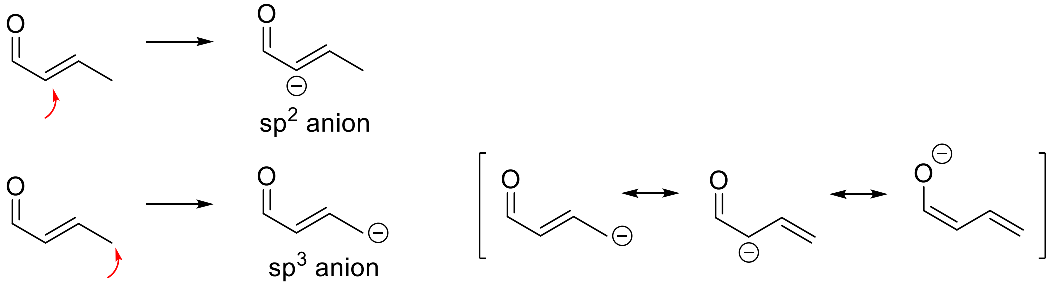

Figure S13. Base deprotonation (red arrow) at the sp^2 α-C and the sp^3 γ-C can both yield a C_4 α-enolate (i.e., the position of origin for the nucleophilic attack), but the sp^2 anion is a much less kinetically favorable intermediate given that, unlike in the sp^3 anion, the negative charge cannot be stabilized via π-delocalization.[37,38]

Table S5. Computational details for NBO analysis of the γ-deprotonated 2-butenal enolate intermediate

<u>2-butenal anion</u>

Input

```
--------------------------------------------------------------------
 # opt freq=noraman b3lyp/6-311+g(d,p) pop=(hirshfeld,nbo,savenbo,full)
  iop(3/33=4) geom=connectivity temperature=523 K
 --------------------------------------------------------------------
```

Optimized Coordinates

O	2.4494930000	-0.1813350000	-0.0000690000
C	1.2894070000	0.2994230000	0.0000050000
C	0.0547690000	-0.3632050000	0.0001200000
C	-1.1812060000	0.3355680000	0.0000230000
C	-2.4598420000	-0.1465200000	-0.0000740000
H	1.1896710000	1.4175020000	0.0000090000
H	0.0583250000	-1.4524340000	0.0001180000
H	-1.0791560000	1.4255550000	0.0001290000
H	-2.6689390000	-1.2132640000	-0.0000550000
H	-3.3146090000	0.5217230000	-0.0000990000

Energies	**Units: [Hartree/Particle]**
Zero-point correction=	0.075262
Thermal correction to Energy=	0.089114
Thermal correction to Enthalpy=	0.090771
Thermal correction to Gibbs Free Energy=	0.018868
Sum of electronic and zero-point Energies=	-230.659044
Sum of electronic and thermal Energies=	-230.645192
Sum of electronic and thermal Enthalpies=	-230.643535
Sum of electronic and thermal Free Energies=	-230.715438

Table S5, continued

Summary of Natural Population Analysis:

```
                          Natural Population
           Natural  -----------------------------------------------
  Atom  No    Charge        Core      Valence    Rydberg      Total
 -----------------------------------------------------------------------
    O    1   -0.74869     1.99979    6.73043    0.01847     8.74869
    C    2    0.29628     1.99923    3.66231    0.04218     5.70372
    C    3   -0.47386     1.99906    4.44793    0.02688     6.47386
    C    4   -0.18090     1.99919    4.16224    0.01947     6.18090
    C    5   -0.60709     1.99926    4.57968    0.02814     6.60709
    H    6    0.05467     0.00000    0.93997    0.00535     0.94533
    H    7    0.17260     0.00000    0.82174    0.00565     0.82740
    H    8    0.16064     0.00000    0.83405    0.00531     0.83936
    H    9    0.16273     0.00000    0.83484    0.00243     0.83727
    H   10    0.16361     0.00000    0.83442    0.00197     0.83639
 =======================================================================
   * Total *   -1.00000     9.99653   27.84762    0.15585    38.00000
```

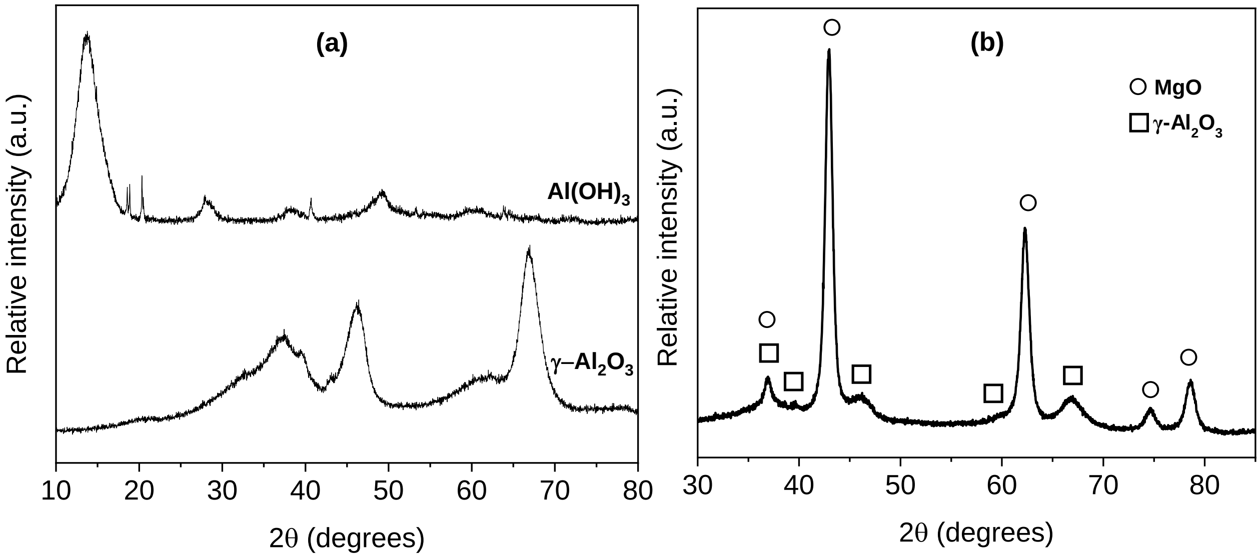

Figure S14. (a) XRD patterns for as-synthesized Al(OH)$_3$ and γ-Al$_2$O$_3$ obtained upon calcination.[18,39] (b) XRD pattern of the mechanical mixture prepared with MgO and γ-Al$_2$O$_3$ with a molar ratio of Mg/Al = 2.

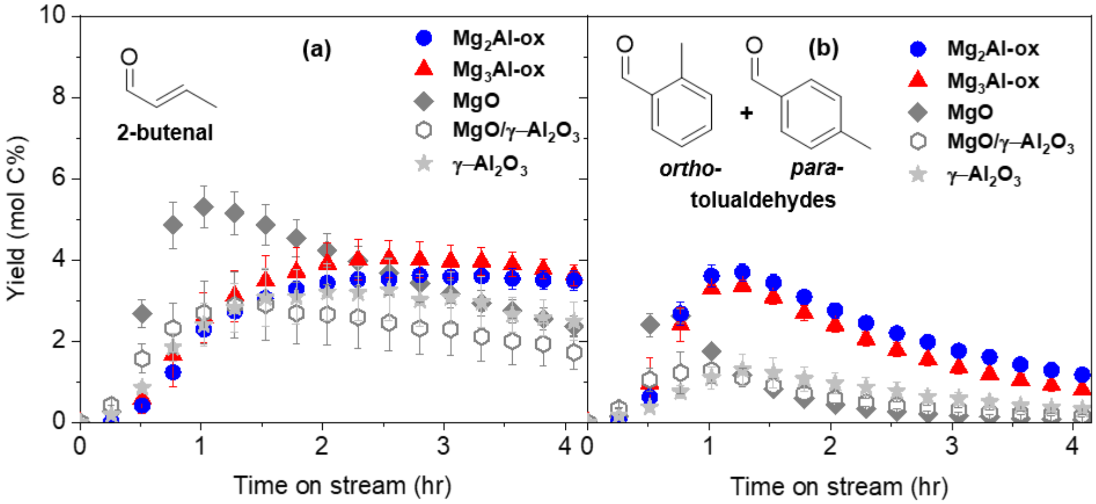

Figure S15. Yields of (a) 2-butenal and (b) tolualdehydes over MgO, Mg$_x$Al-ox, γ-Al$_2$O$_3$, and a mechanical mixture of MgO/γ-Al$_2$O$_3$ (6.13 mg MgO, 3.87 mg γ-Al$_2$O$_3$) with molar Mg/Al = 2 (0.1% acetaldehyde/99.9% N$_2$, 10 sccm total flowrate, 10 mg catalyst, 250 ˚C, 1 bar).

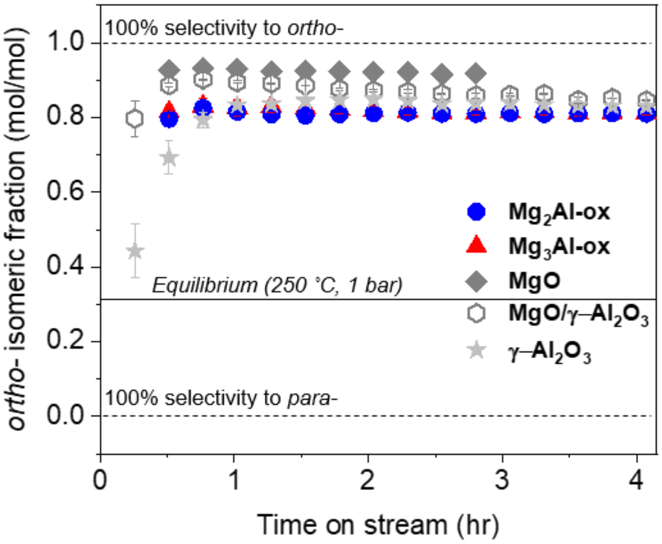

Figure S16. The *ortho*-tolualdehyde isomeric fraction measured over all catalysts investigated: MgO, Mg_xAl-ox, γ-Al_2O_3, and a mechanical mixture of MgO/γ-Al_2O_3 (6.13 mg MgO, 3.87 mg γ-Al_2O_3) with molar Mg/Al = 2 (0.1% acetaldehyde/99.9% N_2, 10 sccm total flowrate, 10 mg catalyst, 250 ˚C, 1 bar).

References

1 P. Lorz, F. Towae, W. Enke, R. Jäckh, N. Bhargava and W. Hillesheim, *Ullmann's Encycl. Ind. Chem.*, 2012, **27**, 35–154.

2 R. A. F. Tomas, J. C. M. Bordado and J. F. P. Gomes, *Chem. Rev.*, 2013, **113**, 7421–7469.

3 S. V. Cherepanova, N. N. Leont'eva, A. B. Arbuzov, V. a. Drozdov, O. B. Belskaya and N. V. Antonicheva, *J. Solid State Chem.*, 2015, **225**, 417–426.

4 T. Sato, K. Kato, T. Endo and M. Shimada, *React. Solids*, 1986, **2**, 253–260.

5 J. I. Di Cosimo, V. K. Díez, M. Xu, E. Iglesia and C. R. Apesteguía, *J. Catal.*, 1998, **178**, 499–510.

6 J. C. A. A. Roelofs, J. A. van Bokhoven, A. J. van Dillen, J. W. Geus and K. P. de Jong, *Chem. A Eur. J.*, 2002, **8**, 5571–5579.

7 J. Shen, M. Tu and C. Hu, *J. Solid State Chem.*, 1998, **137**, 295–301.

8 L. Baggetto, P. Ganesh, C.-N. Sun, R. A. Meisner, T. A. Zawodzinski and G. M. Veith, *J. Mater. Chem. A*, 2013, **1**, 7985–7994.

9 D. H. K. Jackson, B. J. O'Neill, J. Lee, G. W. Huber, J. A. Dumesic and T. F. Kuech, *ACS Appl. Mater. Interfaces*, 2015, **7**, 16573–16580.

10 K. S. W. Sing, D. H. Everett, R. A. W. Haul, L. Moscou, R. A. Pierotti, J. Rouquérol, T. Siemieniewska, J. Rouquerol and T. Siemieniewska, *Pure Appl. Chem.*, 1985, **57**, 603–619.

11 F. Prinetto, G. Ghiotti, P. Graffin and D. Tichit, *Microporous Mesoporous Mater.*, 2000, **39**, 229–247.

12 D. Meloni, R. Monaci, V. Solinas, A. Auroux and E. Dumitriu, *Appl. Catal. A Gen.*, 2008, **350**, 86–95.

13 P. Kustrowski, L. Chmielarz, E. Boz, P. Kus, M. Sawalha and F. Roessner, *Mater. Res. Bull.*, 2004, **39**, 263–281.

14 W. T. Reichle, S. Y. Kang and D. S. Everhardt, *J. Catal.*, 1986, **101**, 352–359.

15 H. Tamura, K. Mita, A. Tanaka and M. Ito, *J. Colloid Interface Sci.*, 2001, **243**, 202–207.

16 E. Kanezaki, *Mater. Res. Bull.*, 1998, **33**, 773–778.

17 T. S. Stanimirova, I. Vergilov and G. Kirov, *J. Mater. Sci.*, 1999, **34**, 4153–4161.

18 J. Shen, J. M. Kobe, Y. Chen and J. A. Dumesic, *Langmuir*, 1994, **10**, 3902–3908.

19 J. Sirita, S. Phanichphant and F. C. Meunier, *Anal. Chem.*, 2007, **79**, 3912–3918.

20 W. Ji, Y. Chen and H. H. Kung, *Appl. Catal. A Gen.*, 1997, **161**, 93–104.

21 Y.-C. Chang and A.-N. Ko, *Appl. Catal. A Gen.*, 2000, **190**, 149–155.

22 E. Dumitriu, V. Hulea, C. Chelaru, C. Catrinescu, D. Tichit and R. Durand, *Appl. Catal. A Gen.*, 1999, **178**, 145–157.

23 H. Idriss, K. S. Kim and M. A. Barteau, *J. Catal.*, 1993, **139**, 119–133.

24 W. Shen, G. a. Tompsett, R. Xing, W. C. Conner and G. W. Huber, *J. Catal.*, 2012, **286**, 248–259.

25 J. E. Rekoske and M. A. Barteau, *Langmuir*, 1999, **15**, 2061–2070.

26 A. K. P. Mann, Z. Wu, F. C. Calaza and S. H. Overbury, *ACS Catal.*, 2014, **4**, 2437–2448.

27 E. Garrone, D. . Bartalini, S. Coluccia, G. Martra, D. Tichit and F. Figueras, *Stud. Surf. Sci. Catal.*, 1994, **90**, 183–193.

28 H. Idriss, C. Diagne, J. P. Hindermann, A. Kiennemann and M. A. Barteau, *J. Catal.*, 1995, **155**, 219–237.

29 V. L. Sushkevich, I. I. Ivanova, V. V Ordomsky and E. Taarning, *ChemSusChem*, 2014, **7**, 2527–36.

30 W. E. Taifan, G. X. Yan and J. Baltrusaitis, *Catal. Sci. Technol.*, 2017, **7**, 4648–4668.

31 D. A. Hickman and L. D. Schmidt, *J. Catal.*, 1992, **282**, 267–282.

32 A. M. Hernández-Giménez, J. Ruiz-Martínez, B. Puértolas, J. Pérez-Ramírez, P. C. A. Bruijnincx and B. M. Weckhuysen, *Top. Catal.*, 2017, **60**, 1522–1536.

33 H. Kurokawa, M. Yanai, M. Ohshima and H. Miura, 2012, **105**, 401–412.

34 V. V. Ordomsky, V. L. Sushkevich and I. I. Ivanova, *J. Mol. Catal. A Chem.*, 2010, **333**, 85–93.

35 V. K. Díez, C. R. Apesteguía and J. I. Di Cosimo, *Catal. Today*, 2000, **63**, 53–62.

36 J. I. Di Cosimo, V. K. Díez, C. Ferretti and C. R. Apesteguía, *Catalysis*, 2014, **26**, 1–28.

37 J. E. Bartmess and J. P. Kiplinger, *J. Org. Chem.*, 1986, **51**, 2173–2176.

38 I. Iriarte, O. Olaizola, S. Vera, I. Gamboa, M. Oiarbide and C. Palomo, *Angew. Chemie - Int. Ed.*, 2017, **56**, 8860–8864.

39 L. Samain, A. Jaworski, M. Edén, D. M. Ladd, D. K. Seo, F. Javier Garcia-Garcia and U. Häussermann, *J. Solid State Chem.*, 2014, **217**, 1–8.